ARTICLE

BIOTECHNOLOGY and BIOENGINEERING

Secondary Flow Mixing Due to Biofilm Growth in Capillaries of Varying Dimensions

Jennifer A. Hornemann,[1,2] Sarah L. Codd,[2,3] Robert J. Fell,[1] Philip S. Stewart,[1,2] Joseph D. Seymour[1,2]

[1]Department of Chemical & Biological Engineering, Montana State University, Bozeman, Montana

[2]Center for Biofilm Engineering, Montana State University, Bozeman, Montana

[3]Department of Mechanical Engineering, Montana State University, Bozeman, Montana; telephone: 406-994-1944; fax: 406-994-6292; e-mail: scodd@coe.montana.edu

Received 10 October 2008; revision received 22 December 2008; accepted 29 December 2008

Published online 28 January 2009 in Wiley InterScience (www.interscience.wiley.com). DOI 10.1002/bit.22248

ABSTRACT: Using a magnetic resonance microscopy (MRM) technique, velocity perturbations due to biofouling in capillaries were detected in 3D velocity maps. The velocity images in each of the three square capillary sizes (2, 0.9, and 0.5 mm i.d.) tested indicate secondary flow in both the *x*- and *y*-directions for the biofouled capillaries. Similar flow maps generated in a clean square capillary show only an axial component. Investigation of these secondary flows and their geometric and dynamic similarity is the focus of this study. The results showed significant secondary flows present in the 0.9 mm i.d. capillary, on the scale of 20% of the bulk fluid flow. Since this is the "standard 1 mm" size capillary used in confocal microscopy laboratory bioreactors to investigate biofilm properties, it is important to understand how these enhanced flows impact bioreactor transport.

Biotechnol. Bioeng. 2009;103: 353–360.

KEYWORDS: magnetic resonance imaging; biofilm; transport; capillary; NMR

Introduction

Control of mixing and transport in capillary bioreactors and biofouled capillary membranes is an important engineering challenge in industrial and biomedical systems. *Staphylococcus epidermidis* is a Gram-positive, coagulase negative member of the bacterial genus *Staphylococcus*. Commonly found on human skin, *S. epidermidis* is the most common species used in laboratory tests. *S. epidermidis* is a main cause of infection in patients with medical implants (Costerton et al., 2005). Unfortunately for these patients, *S. epidermidis* biofilms are resistant to most common antibiotics (Brock et al., 1994). These troublesome microcolonies primarily consist of bacterial cells and extracellular polymeric substance (EPS). Early studies indicated that the EPS attaches to a surface by the way of adhesive polysaccharides excreted by the cells (Costerton, 1999), but more recently EPS is known to be a conglomeration of many biopolymers (Sutherland, 2001). EPS may account for 50–90% of the total organic carbon of biofilms and can be considered the primary matrix material (Xavier et al., 2005). The EPS matrix hydrogel is important when studying biofilm transport properties in square capillaries due to its viscoelastic behavior (Rupp et al., 2005; Shaw et al., 2004; Stoodley et al., 1994; Towler et al., 2007).

This study presents magnetic resonance microscopy (MRM) data for testing and development of bioreactor system transport models. Biofilms were imaged in their natural state allowing for accurate study of their structure and impact on advective transport. This non-invasive technique allows images to be taken of biofilms in an environment similar to their native environment (Gjersing et al., 2005; Seymour et al., 2004a). Biofilms can be grown in capillaries of various sizes using similar techniques. Using standard protocols for growing capillary biofilms to be imaged using a confocal microscope (Rani et al., 2005), the resulting biofilm thickness is 10–20% of capillary cross-section where the growth period varies according to capillary size. MRM is a unique tool for measuring

The presence of spatially varying secondary flows generated by the heterogeneous biofilm plays a role in the spatial distributing of biological function through varying speciation and chemical communication. The data presented show reactor size impacts studies of spatially distributed biological activity and the idea that scaling of transport models in biofilm impacted devices is possible.

Correspondence to: S.L. Codd

Contract grant sponsor: NIH
Contract grant number: NIH P20 RR016455-04
Contract grant sponsor: NSF
Contract grant numbers: NSF CAREER Award 0642328; NSF CAREER Award 03480076
Contract grant sponsor: DOE Office of Science Biological Environmental Research ERSP
Contract grant number: DOE ERSP DE-FG02-07-ER-64416

quantitative flow maps and transport parameters, and allows determination of similitude conditions (Bird et al., 2002) in different-sized systems where similar flow characteristics exist.

Classical approaches to interfacial transport using an empirical mass transfer coefficient proportional to power law scaling of the Reynolds and Schmidt numbers (Bird et al., 2002) do not capture the role of secondary flows. The spatial variation of advective transport generates a spatially heterogeneous rate of mass flux in the capillary system. In the case of biomedical separations, for example, blood filtration, which uses capillary membranes, these variations can result in spatially varying driving forces and contaminant concentration. The square capillaries used in this work (Gjersing et al., 2005) are used extensively in confocal microscopy studies (Rani et al., 2005; Stewart et al., 2007; Takenaka et al., 2008) of fluorescent biomolecular binding. Previous studies on spatial variation of genetic and metabolic biofilm behavior (Kirisits et al., 2007; Majors et al., 2005a,b; McLean et al., 2008a,b) are impacted by the flow behaviors elucidated here. Of broader engineering interest is the impact of soft interfaces on mixing and transport in a range of systems (de Gennes, 1994; Debeer et al., 1994; Pathak et al., 2004; Qi and Hou, 2006; Ziebis, 1996), and the results of this work are discussed in that context.

MRM is a non-invasive tool able to access several observable quantities in biofilms such as chemical composition (Majors et al., 2005a; Vogt et al., 2000), diffusion (Hornemann et al., 2008), and macroscale structure and transport (Gjersing et al., 2005; Manz et al., 2005; Seymour et al., 2004a,b). This research uses MRM to characterize velocity profiles for flow in capillary bioreactors. It was found that the presence of biofilms in capillary reactors generates significant secondary flows in the non-axial directions and that the orthogonal components of these secondary flows tend to be out of phase (Gjersing et al., 2005). Additionally, MRM has been shown to characterize a biofilm's internal structure by revealing the contrast in density, via T_2 relaxation (Hoskins et al., 1999; Lewandowski et al., 1992; Manz et al., 2003) throughout the biofilm (Gjersing et al., 2005; Seymour et al., 2004a). T_2 is a nuclear spin relaxation time, which varies depending on molecular rotational freedom and is typically shorter for more viscous fluids or more solid-like materials such as gels, for example, biofilms. These same studies indicated that the generation of significant secondary flows by biofilms can require modification of current mass transport models (Beyenal and Lewandowski, 2002; Chambless et al., 2006; Eberl et al., 2000; Horn and Hempel, 1997; Lewandowski and Beyenal, 2003; Picioreanu et al., 2000a,b) for transport from the bulk fluid to the biofilm (Gjersing et al., 2005).

Theory

Many unique biofilm features have not been sufficiently characterized by experimental data. An area of particular interest to biomedical researchers is bioreactor fluid dynamics because of its applications to certain biomedical devices, clinical procedures, and research on biomolecular microbiology of biofilms. More insight into biofilm properties and their impact on fluid flow could prove beneficial to the design of implanted biomedical devices that commonly become infected with biofilm-forming bacteria and in bioseparation devices. MRM has proven to be an informative bioreactor experimental technique. Its ability to produce accurate images of changes in the biofilm structure and reactor transport non-invasively provides unique experimental data (Gjersing et al., 2005; Hoskins et al., 1999; Lewandowski et al., 1992; Manz et al., 2003; Seymour et al., 2004a).

Transport Impacted by Biofilm Growth

Confocal microscopy is a prominent experimental tool to analyze microbial biofilm spatial structure (Nivens et al., 2001; Stoodley et al., 1994) and spatially distributed biological activity (Debeer et al., 1994; Heydorn et al., 2002). A typical biofilm confocal microscopy study uses a 1.0 mm o.d. with a 0.9 mm i.d. square cross-section capillary bioreactor (Kirisits et al., 2007; Rupp et al., 2005; Stewart et al., 2007). The transport of biomolecules, composing nutrients, metabolites, RNA, DNA proteins, and enzymes, depends on the interaction between the free stream velocity field and the biofilm biomass. The relative amplitude of advective and diffusive transport mechanisms varies as a function of spatial location. The presence of spatially varying secondary flows generated by the heterogeneous biofilm potentially plays a role in the spatial distribution of biological function through spatial distribution of microbe genetic variation and chemical communication (Heydorn et al., 2002). In classical mass transfer approaches, mass transfer coefficients dependent on Reynolds number correlations based on the bulk axial velocity v_z are used (Bird et al., 2002; Gjersing et al., 2005; Lewandowski and Beyenal 2007; Lewandowski et al., 1995). In non-turbulent ($Re < 2100$) systems where temporally or spatially irregular boundary conditions generate secondary flows with non-zero, non-axial v_x and v_y velocity components, the classical theory fails to account for spatially dependent advective mixing and transport (Gjersing et al., 2005). In turbulent ($Re > 2100$) flow transport theory, models incorporate additional turbulent fluxes resulting from fluctuations in point velocity about the mean (Bird et al., 2002). Such approaches also do not capture the physics associated with the transport processes in capillary bioreactors. The data presented here indicate that due to the presence of significant secondary flows, full solution of the velocity field is needed to quantifiably model mass transport (Picioreanu et al., 2000b). Significant work along these lines is being undertaken (Kapeloos et al., 2006; Picioreanu et al., 2000a).

Biofilms represent a viscoelastic surface perturbation, which is heterogeneous both in biopolymer spatial

distribution and hence material response. An interesting question in scale up or down of bioreactor systems is the role of such a fixed thickness perturbation as the reactor system dimension varies. The concept of dynamic similitude in fluid dynamics implies that for the same Reynolds number in similar geometries the dynamics are reproducible (Bird et al., 2002). A classic example is the Taylor–Couette hydrodynamic instability for fluid flow in the gap of two concentric cylinders with the inner cylinder rotating. Above a critical rotation rate, secondary flow in the radial v_r and axial v_z directions is generated as a perturbation on the primary angular v_θ flow (Chandrasekhar, 1981). The wavelength of the secondary axial flow velocity scales with cylinder gap at similar Reynolds number indicating dynamic similitude.

Materials and Methods

Growing Biofilms

The stages of growing a *S. epidermidis* biofilm include setting up the bioreactor system, growth of suspended bacterial cells, inoculation of the bioreactor system, and a monitored growth period. An initial liquid culture was prepared using 10 mL of 30 $g\,L^{-1}$ tryptic soy broth (TSB; Difco Becton–Dickinson, Sparks, MD) and *S. epidermidis* cells from frozen stock (−70°C) ATCC# 35984. Both were mixed in a micro centrifuge tube, and the suspended bacteria cells were shaken at 37°C overnight (12 h). Once the suspended bacterial cells reach a desired concentration as determined by the optical density measured with a spectrophotometer at 600 nm, the solution was used to inoculate the bioreactor system.

The bioreactor is gravity fed with a nutrient solution of 30 g TSB per 10 L of water and Magnevist (20 mL of pure Magnevist per 500 mL of DI H_2O). Magnevist (Berlex Laboratories, Mfd., Wayne, NJ) reduces the necessary MRM experiment duration by decreasing T_1 relaxation and allowing more rapid signal acquisition, and due to chelating does not penetrate cell membranes. At the concentrations used, Magnevist has been shown not to affect biofilm growth (Lewandowski et al., 1992). The system components consist of a square capillary (Friedrich and Dimmock, Millville, NJ) bioreactor in a protective glass casing, two 10 L carboys (one for feed and one for waste), an incubator set at 37°C which provides optimal conditions for biofilm growth, a glass flow break upstream of the capillary bioreactor that maintains steady-state flow, and an inoculation chamber downstream of the capillary. The area upstream and downstream of the square capillary was clamped to prevent flow for a 4 h period after inoculation. This time allows the bacteria cells to "settle" onto the capillary walls whilst it is in a horizontal position. In order to maximize biofilm properties for MRM experiments, the biofilm was fed nutrient at a fixed flow rate of 16.7 $mL\,s^{-1}$ using a peristaltic pump ($Re = 8$–33) for 48–96 h depending on capillary size. Shear during growth is important in determining the resultant mechanical properties of a biofilm (Stoodley et al., 1994). Therefore, flow rates and *Re* were kept as fixed as possible during biofilm growth. During MR experiments, the constant flow rate was controlled with a gravitational head to eliminate peristaltic pump vibrations and to maintain velocities within the desired MR measurement window. Flow rates during MR experiments varied depending on capillary size: $Re = 110 \pm 3.8$ for the 2 mm capillary, $Re = 430 \pm 30$ for the 0.9 mm capillary, and $Re = 562 \pm 172$ for the 0.5 mm capillary. This study focuses on six biofilm experiments; there were two for each of following capillary cross-section lengths: 2, 0.9, and 0.5 mm. At the end of the growth period, the bioreactor system was transferred into the MRM instrument.

MRM Biofilm Experiments

MRM measurements are made using a Bruker DRX spectrometer ($B_0 = 5.9$ T), a 5-mm saddle radio frequency coil, and magnetic field gradients up to 1.7 $T\,m^{-1}$. For each capillary size, velocity maps were taken using a velocity phase encoding pulse sequence (Callaghan, 1991) shown in Figure 1 and a specific set of experimental parameters.

The sequence combines a standard spin warp magnetic resonance imaging (MRI) sequence with the basic pulsed gradient spin echo (PGSE) experiment and is used to measure translational spin displacement over a specific time interval Δ with a magnetic gradient pair applied for a time δ (Callaghan, 1991; Fukushima, 1999). This ordering of rf pulses, magnetic field gradients, and data acquisition is used to examine position exchange (Blumich, 2000). The first gradient encodes for position, r, waiting a time Δ for the spins to move, and using a second gradient to encode for the new position, r'. The signal is then encoded for displacements $(r' - r)$. Knowing the spin displacement over a fixed time interval Δ allows for velocity calculations from the net phase shift of the magnetization (Blumich and Kuhn, 1992; Callaghan, 1991). Two images are taken, the first image without motion encoding PGSE gradients ($g = 0$ $mT\,m^{-1}$),

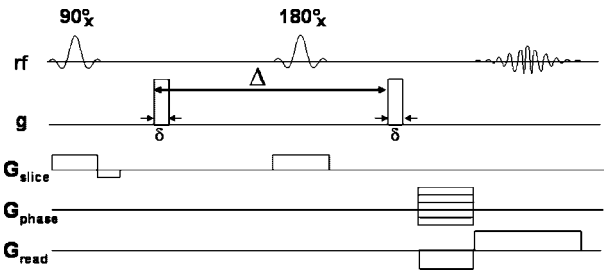

Figure 1. Pulse sequence used to make displacement measurements and create velocity maps.

and the second image with PGSE gradient values ranging from 150 to 800 mT m^{-1}. Depending on the capillary size, various gradients were required due to the range of velocities present. The gradients for each of the sizes were 800 mT m^{-1} for the 2 mm, 300 mT m^{-1} for the 0.9 mm, and 150 mT m^{-1} for the 0.5 mm capillary. The phase difference, Φ, for each pixel between the images is dependent on the velocity v in that pixel via $\Phi = 2\pi/\gamma\delta\Delta v$, where δ is the time the gradient is applied and Δ is the delay time between gradients. For our experiments $\delta = 1$ ms, $\Delta = 10$ ms, the repetition time was 500 ms, the echo time was 17.9 ms, and four averages were used. The velocity images were averaged over a 0.3-mm slice thickness. All three velocity components v_x, v_y, and v_z were measured with a total experimental time varying from 51 min for the 0.5 mm up to 90 min for the 2 mm capillary. This timescale is short relative to biological growth timescales, and any sloughing events would manifest themselves as image artifacts and were not detected. The experiments used a spatial orientation: the read gradient in z-direction, the phase gradient in x-direction, and the slice gradient in the y-direction. The magnetic field gradients applied give spatial resolution of the (x,z) plane over the 0.3 mm slice in y-direction, where the z-axis is the long axis of the capillary. The velocity profiles measured are bulk flow $v_z(x,z)$, the cross-stream x- and y-directions, $v_x(x,z)$ and $v_y(x,z)$. The field of view (FOV) decreased with capillary size: 20 mm × 3 mm for the 2 mm capillary, 20 mm × 2.5 mm for the 0.9 mm capillary, and 20 mm × 1.5 mm for the 0.5 mm capillary. Using 128 × 64 pixels, the resulting spatial resolution was 156 × 47 μm pixel^{-1} for the 2 mm capillary, 156 × 39 μm pixel^{-1} for the 0.9 mm capillary, and 156 × 23 μm pixel^{-1} for the 0.5 mm capillary.

All of the data presented in this article address the known variations in biological samples by performing multiple experiments, averaging the results, and reporting the trends.

Results and Discussion

The velocity profile for clean capillaries (no biofilm) shows fastest flow at the capillary mid-section and no flow at the sides (Seymour et al., 2004a), as is typical for laminar flow of a Newtonian fluid through a conduit. Clean capillaries also have no secondary flows v_x, $v_y = 0$. Velocity maps for each capillary size in this study after biofouling are shown in Figures 2–4. Since previous data (Gjersing et al., 2005; Seymour et al., 2004a) indicate significant secondary flow, one of the objectives of this research is to determine if conditions of hydrodynamic similitude, geometric, and dynamic similarity exist in biofouled capillaries. Of particular interest is whether the secondary flow structures scale with capillary length scale despite the fact that the biofilms have an average thickness of the order of 100 μm and occupy a different proportion of the capillary (varies 5–20%) as the capillary cross-sectional length scale is varied.

The velocity profiles in the biofouled capillaries clearly indicate significant non-axial flow components, which exhibit oscillatory flow behavior throughout the capillary

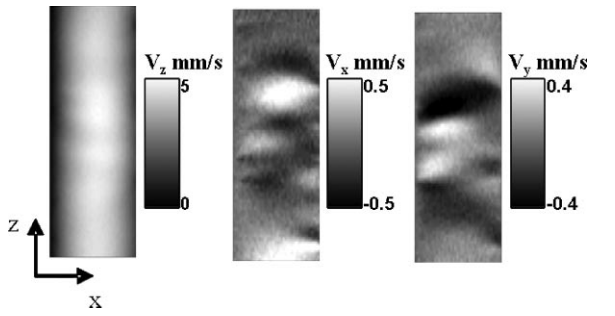

Figure 2. Biofouled 2 mm capillary velocity maps with biofouling on the left side of the capillary. The v_x and v_y components exhibit significant non-axial flow components inside the capillary bioreactor. The slice thickness is 0.3 mm with spatial resolution of 156 × 47 μm pixel^{-1}. FOV shown (2 mm × 11.72 mm) is a cropped section from the entire image and is magnified in the x-direction.

bioreactor (Figs. 2–4) as previously demonstrated for a 0.9 mm capillary (Gjersing et al., 2005; Seymour et al., 2004a). The spatial flow frequencies present were quantified by performing a Fourier transformation (FT) of the data points, after appropriate baseline corrections of a line drawn through the capillary center along the longitudinal axis as indicated in Figure 5. The Fourier transform statistically characterizes the periodicity of the non-axial streamlines. Data in Figure 6 show distinguishable peaks in the FT graphs. By observing the dominant frequency for each size capillary, it is evident that the peak is proportional to the capillary size. For example, in the 2 mm graph, the dominant frequency is 40 mm^{-1} ($\lambda = 2.5$ mm). Scaling down to a 0.9 mm cross-section gives a frequency that is close to

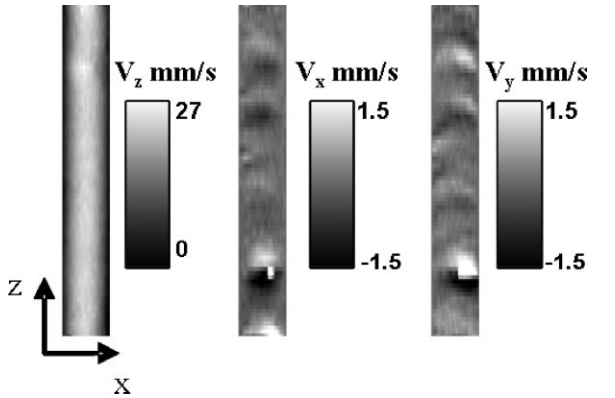

Figure 3. Biofouled 0.9 mm capillary velocity maps with biofouling on the left side of the capillary. There are obvious non-axial flow components inside the capillary bioreactor. The slice thickness is 0.5 mm with a spatial resolution of 156 × 39 μm pixel^{-1}. FOV shown (0.9 mm × 11.72 mm) is a cropped section from the entire image and is magnified in the x-direction. *Note*: A large biofilm cluster is causing some faster velocities and velocity wrapping in a few pixels towards the bottom of the images.

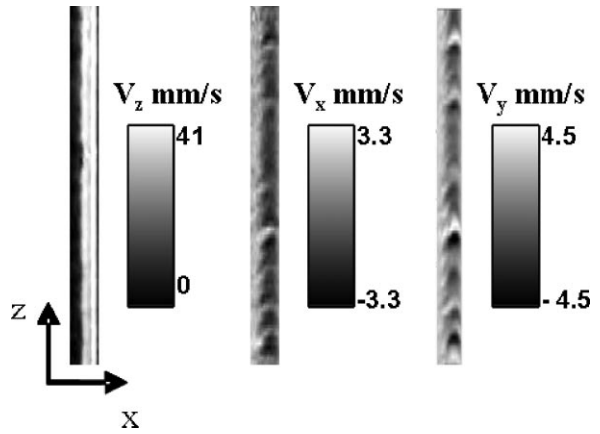

Figure 4. Biofouled 0.5 mm capillary velocity maps with biofouling on the left side of the capillary. Non-axial flow components are apparent in the capillary bioreactor. The slice thickness is 0.3 mm with a spatial resolution of 156×23 μm pixel^{-1}. FOV shown (0.5 mm $\times$ 11.72 mm) is a cropped section from the entire image and is magnified in the *x*-direction. Note that this narrow capillary was slightly misaligned with the gradient axis and hence v_x and v_y show a small baseline component due to the large axial flow that was removed before FT analysis.

80 mm^{-1} ($\lambda = 1.25$ mm). Likewise, for the 0.5 mm capillary, the dominant frequency is found at 160 mm^{-1} ($\lambda = 0.625$ mm). The ratio of the wavelength to channel width is 1.25 ± 0.14 for all three capillary sizes.

Averaging the maximum non-axial velocity observed at the capillary centerline for multiple biofilms in the same capillary size allows comparison of the relative amplitude of the secondary flows between the different size capillaries. The secondary flows are most significant at the centerline in the 0.9 mm capillary at approximately 20% of the maximum *z*-direction flow. This appears to be due to the capillary size in combination with the size of the biofilm, a resonant-like effect. That is, in the 2 mm capillary the secondary flows are damped at the centerline by viscosity due to the larger cross-section. While in the 0.5 mm capillary, the upper wall is close enough to the biofilm to cause damping. Table I summarizes an average value for the experimentally observed secondary flow amplitudes at the capillary centerline.

Another comparison of the 2 mm capillary flow data to the values from the 0.9 mm capillaries is shown through analysis of the secondary flows as a function of the distance from the biofilm. The bottom surface inside the capillary is referenced as 0 mm. The top capillary surface is the full inner width. To determine the impact of the biofilm surface on the flow field, several velocity profiles were analyzed at locations above the biofilm surface. T_2 images and the zero flow regions in the velocity maps were used to ensure an average biofilm height of 100 μm for every sample used in this study. A combination of established protocols (Gjersing et al., 2005) were used to estimate the necessary growth time to get the desired (100 μm) thickness, but also checked visually and verified with MR T_2 and velocity maps before using a sample for this study. These locations are shown in Figure 7 for clarification via a schematic. At positions closer to the biofilm–fluid interface in the 2 mm capillary, secondary flows as a percentage of the bulk flow increase to the same order of magnitudes observed in the 0.9 mm capillary. For example, the 0.9 mm centerline is 350 μm from the average biofilm surface where the secondary *x*-direction velocity ratio is approximately 20% for $v_{x,\max}/v_{z,\max}$ and in the 2 mm at similar distance above the average biofilm surface (300 μm), $v_{x,\max}/v_{z,\max}$ is 22.65%. The velocity values were not so closely related in the *y*-direction when comparing the same positions (300–350 μm) where the 0.9 mm retained the 20% for $v_{y,\max}/v_{z,\max}$, but only 14% in the 2 mm

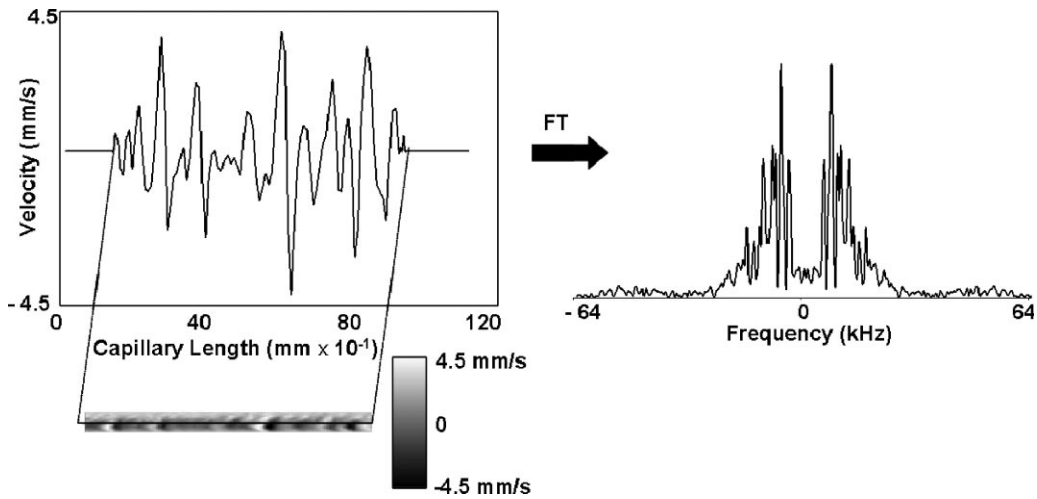

Figure 5. A Fourier transformation (right) of a line through the 0.5 mm velocity map shows the spatial frequencies (mm^{-1}) of the flow through the capillary bioreactor.

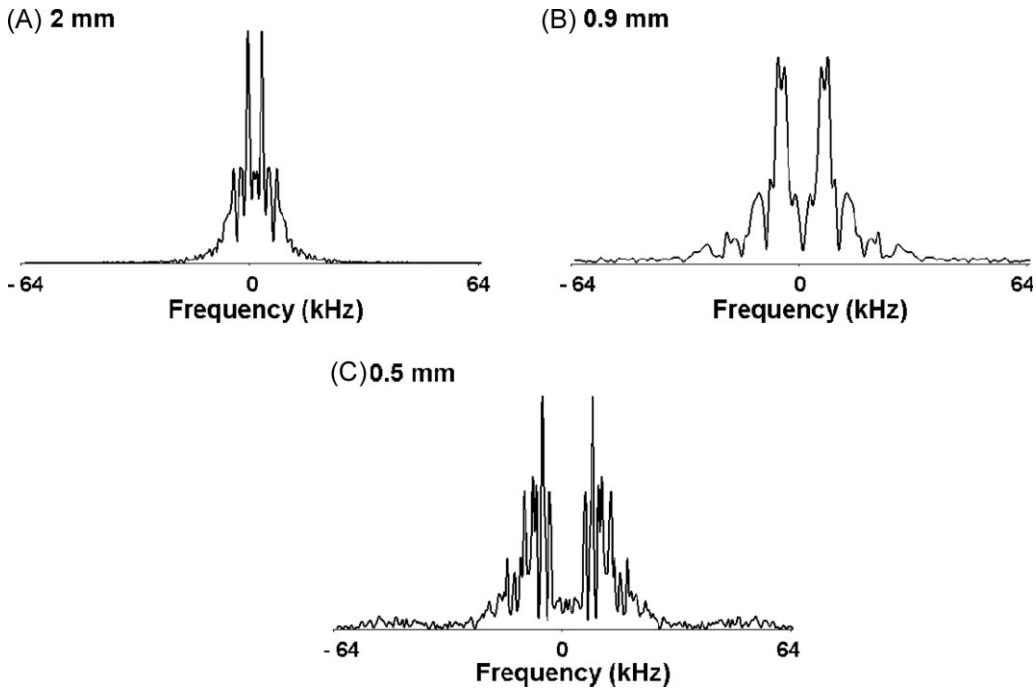

Figure 6. Fourier transformations of velocity data for (**A**) 2 mm, (**B**) 0.9 mm, and (**C**) 0.5 mm capillaries. The strongest peaks at a frequency are inversely related to the capillary cross-section.

indicating asymmetry in the larger capillary. The data clearly indicate that the proportion of the channel width the biofilm occupies impacts the variation in mixing by secondary flow. This leads to the idea that confocal microscopy data on spatial variation of biological function (Heydorn et al., 2002; Kirisits et al., 2007; Nivens et al., 2001) based on data from studies on single bioreactor sizes is prone to reactor size dependency. Table II shows the secondary velocities as a percentage of the axial velocity as data analysis lines move from the centerline towards the biofilm.

Conclusions

This article presents analysis of the dependence of secondary flows generated by biofilms of approximately 100 μm thickness on capillary bioreactor cross-section size. The wavelength of the secondary flows is shown to scale with the capillary bioreactor cross-section in analogy with the scaling of wavelength with Couette gap size in hydrodynamic instabilities like Taylor vortices. However, the amplitude of the secondary flows, represented as a percentage of the bulk axial flow, depends on the distance from the biofilm. The capillary bioreactor cross-section size thus interacts with the biofilm and generates stronger secondary flows at the bioreactor centerline as shown for the 0.9 mm capillary or weaker flows due to solid boundary effects, as in the 0.5 mm capillary or viscous damping as in the 2 mm capillary. The presence of spatially varying secondary flows generated by the heterogeneous biofilm plays a role in the spatial distribution of biological function through varying speciation and chemical communication. The data presented here clearly support the conclusion that reactor size impacts studies of spatially distributed biological activity, and the idea that, scaling of transport models in biofilm impacted devices is possible but requires more study. 2D numerical simulations with either random or periodic solid surfaces did not introduce secondary flows of as large an amplitude as observed in the biofilm samples. Whether the viscoelastic nature of the biofilm or the spatial growth pattern of the biofilm causes the enhanced oscillatory motion observed in the biofouled capillaries is the subject of ongoing experiments on model soft interfacial surfaces. It should be noted that the numerical simulation of fluid dynamics with soft viscoelastic interfacial boundary conditions is an open topic of research. The biological impact of these secondary flows

Table I. The *x*- and *y*-direction average maximum velocity as a percentage of the maximum *z*-direction velocity for the three different capillary cross-sections.

	0.5 mm	0.9 mm	2 mm
$v_{x,\max}/v_{z,\max} \times 100$	4.9 ± 0.1	20 ± 0.3	12 ± 2.8
$v_{y,\max}/v_{z,\max} \times 100$	5.6 ± 0.9	21 ± 4.3	8.7 ± 2.2

Data are taken from the centerline of the capillary. The biofilm surface has a different impact on the flow depending on capillary size. The biggest impact is in the 0.9 mm capillary where the biofilm occupies approximately 11% of the capillary inner cross-section.

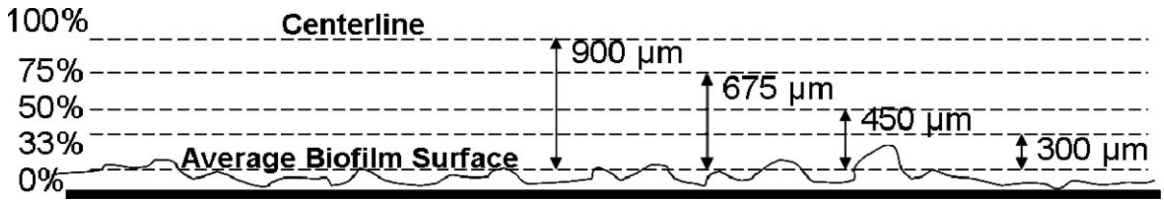

Figure 7. Schematic explaining the data analysis process of choosing velocity profiles at various distances from the average biofilm surface–liquid interface in 2 mm capillary.

Table II. The percentage maximum x- and y-direction flow of the maximum z-direction flow to relate distance from fluid–biofilm interface to secondary flow significance.

Vertical capillary position	$v_{x,\max}/v_{z,\max} \times 100$	$v_{y,\max}/v_{z,\max} \times 100$
0.9 mm centerline (350 μm to biofilm surface)	20	21
2 mm (300 μm to biofilm surface)	23	14
2 mm (450 μm to biofilm surface)	18	13
2 mm (675 μm to biofilm surface)	16	11
2 mm centerline	12	8.7

The average biofilm–fluid interface is designated as 100 μm with distance increasing towards the 1.0 mm centerline to a maximum of 900 μm from the biofilm. Both non-axial flow ratios are significant and, in particular, the x component in both the 0.9 mm and 2 mm capillaries shows the same magnitude in the 300–400 μm range from the biofilm surface independent of capillary dimension. Since the biofilm grows asymmetrically perpendicular to the x-direction, the y-component may be more of a function of capillary size.

is also an open question as they induce spatially variable advection of nutrients and the biofilm structure may assist in optimizing this transport.

Nomenclature

B_0	external magnetic field (T)
g_i	magnetic field gradient for motion sensitivity ($\mathrm{T\,m^{-1}}$)
G_i	magnetic field gradient in the i direction ($\mathrm{T\,m^{-1}}$)
r	spatial coordinate vector (m)
Re	Reynolds number ($Re = v_{z,\max} l/\nu$)
T_2	transverse, spin–spin relaxation time (s)
v_i, $i = x, y, z, r, \theta$	components of velocity vector ($\mathrm{m\,s^{-1}}$)
$v_{i,\max}$	maximum velocity component ($\mathrm{m\,s^{-1}}$)
x	Cartesian spatial coordinate
y	Cartesian spatial coordinate
z	Cartesian spatial coordinate, axis of capillary

Greek Letters

δ	duration of velocity encoding gradient pulses (s)
Δ	observation time for encoding displacement (s)
γ	gyromagnetic ratio, for protons $\gamma = 2.675\mathrm{E}8$ ($\mathrm{rad\,s^{-1}\,T^{-1}}$)
ν	kinematic viscosity ($\mathrm{m^2\,s^{-1}}$)
Φ	phase difference (rad)

J.H. and R.F. acknowledge the support of NIH Grant Number P20 RR016455-04 from the INBRE-BRIN Program of the NCRR NIH, and its contents are solely the responsibility of the authors and do not necessarily represent the official view of NCRR or NIH. S.L.C. acknowledges the support of a NSF CAREER Award 0642328. J.D.S. acknowledges the support from an NSF CAREER Award 03480076. J.D.S. and S.L.C. acknowledge the support from the DOE Office of Science Biological Environmental Research ERSP Grant DE-FG02-07-ER-64416 and equipment grants from NSF MRI and the Murdock Trust. The authors thank Betsey Pitts at the Center for Biofilm Engineering, MSU, for assistance with biofilm growth and Tyler Brosten for helpful discussions.

References

Beyenal H, Lewandowski Z. 2002. Internal and external mass transfer in biofilms grown at various flow velocities. Biotechnol Prog 18: 55–61.

Bird RB, Stewart WE, Lightfoot EN. 2002. Transport phenomena. New York: John Wiley & Sons, Inc.

Blumich B. 2000. NMR imaging of materials. Oxford: Clarendon Press.

Blumich B, Kuhn W, editors. 1992. Magnetic resonance microscopy: Method and application in materials science, agriculture and biomedicine. New York: VCH.

Brock TD, Madigan MT, Martinko JM, Parker J. 1994. Biology of microorganisms. NJ: Prentice-Hall.

Callaghan PT. 1991. Principles of nuclear magnetic resonance microscopy. New York: Oxford Clarendon Press.

Chambless JD, Hunt SM, Stewart PS. 2006. A three-dimensional computer model of four hypothetical mechanisms protecting biofilms from antimicrobials. Appl Environ Microbiol 72(3):2005–2013.

Chandrasekhar S. 1981. Hydrodynamic and hydromagnetic stability. New York: Dover.

Costerton JW. 1999. Introduction to biofilm. Int J Antimicrob Agent 11:217–221.

Costerton JW, Montanaro L, Arciola CR. 2005. Biofilm in implant infections: Its production and regulation. Int J Artif Organs 28(11):1062–1068.

de Gennes PG. 1994. Soft interfaces. Paris: Cambridge University Press.

Debeer D, Stoodley P, Roe F, Lewandowski Z. 1994. Effects of biofilm structures on oxygen distribution and mass-transport. Biotechnol Bioeng 43(11):1131–1138.

Eberl HJ, Picioreanu C, Heijnen JJ, van Loosdrecht MCM. 2000. A three-dimensional numerical study on the correlation of spatial structure, hydrodynamic conditions, and mass transfer and conversion in biofilms. Chem Eng Sci 55:6209–6222.

Fukushima E. 1999. Nuclear magnetic resonance as a tool to study flow. Ann Rev Fluid Mech 31:95–123.

Gjersing EL, Codd SL, Seymour JD, Stewart PS. 2005. Magnetic resonance microscopy analysis of advective transport in a biofilm reactor. Biotechnol Bioeng 89(7):822–834.

Heydorn A, Ersboll B, Kato J, Hentzer M, Parsek MR, Tolker-Nielsen T, Givskov M, Molin S. 2002. Statistical analysis of *Pseudomonas aeruginosa* biofilm development: Impact of mutations in genes involved in twitching motility, cell-to-cell signaling, and stationary-phase sigma factor expression. Appl Environ Microbiol 68(4):2008–2017.

Horn H, Hempel DC. 1997. Substrate utilization and mass transfer in an autotrophic biofilm system: Experimental results and numerical solution. Biotechnol Bioeng 53(4):363–371.

Hornemann JA, Lysova AA, Codd SL, Seymour JD, Busse SC, Stewart PS, Brown JR. 2008. Biopolymer and water dynamics in microbial biofilm extracellular polymeric substance. Biomacromolecules 9(9):2322–2328.

Hoskins BC, Fevang L, Majors PD, Sharma MM, Georgiou G. 1999. Selective imaging of biofilms in porous media by NMR relaxation. J Magn Reson 139(1):67–73.

Kapeloos GE, Alexiou TS, Payatakes AC. 2006. Hierarchical simulator of biofilm growth and dynamics in granular porous materials. Adv Water Res 30:1648–1667.

Kirisits MJ, Margolis JJ, Purevdorj-Gage BL, Vaughan B, Choop DL, Stoodley P, Parsek MR. 2007. Influence of the hydrodynamic environment on quorum sensing in *Pseudomonas aeruginosa* biofilms. J Bacteriol 189(22):8357–8360.

Lewandowski Z, Beyenal H. 2003. Mass transport in heterogeneous biofilms. In: Wuertz S, Bishop PL, Wilderer PA, editors. Biofilms in wastewater treatment. London: IWA Publishing. p. 147–177.

Lewandowski Z, Beyenal H. 2007. Fundamentals of biofilm research. Boca Raton: CRC Press Inc./Lewis Publishers.

Lewandowski Z, Altobelli SA, Majors PD, Fukushima E. 1992. NMR imaging of hydrodynamics near microbially colonized surfaces. Water Sci Technol 26(3–4):577–584.

Lewandowski Z, Stoodley P, Altobelli S. 1995. Experimental and conceptual studies on mass-transport in biofilms. Water Sci Technol 31(1):153–162.

Majors PD, McLean JS, Fredrickson JK, Wind RA. 2005a. HMR methods for in-situ biofilm metabolism studies: Spatial and temporal resolved measurements. Water Sci Technol 52(7):7–12.

Majors PD, McLean JS, Pinchuk GE, Fredrickson JK, Gorby YA, Minard KR, Wind RA. 2005b. NMR methods for in situ biofilm metabolism studies. J Microbiol Methods 62(3):337–344.

Manz B, Volke F, Goll D, Horn H. 2003. Measuring local flow velocities and biofilm structure in biofilm systems with magnetic resonance imaging (MRI). Biotechnol Bioeng 84(4):424–432.

Manz B, Volke F, Goll D, Horn H. 2005. Investigation of biofilm structure, flow patterns and detachment with magnetic resonance imaging. Water Sci Technol 52(7):1–6.

McLean JS, Majors PD, Reardon CL, Bilskis CL, Reed SB, Romine MF, Fredrickson JK. 2008a. Investigations of structure and metabolism within *Shewanella oneidensis* MR-1 biofilms. J Microbiol Methods 74(1):47–56.

McLean JS, Ona ON, Majors PD. 2008b. Correlated biofilm imaging, transport and metabolism measurements via combined nuclear magnetic resonance and confocal microscopy. ISME J 2(2):121–131.

Nivens DE, Ohman DE, Williams J, Franklin MJ. 2001. Role of alginate and its O acetylation in formation of *Pseudomonas aeruginosa* microcolonies and biofilms. J Bacteriol 193(3):1047–1057.

Pathak JA, Ross D, Migler KB. 2004. Elastic flow instability, curved streamlines, and mixing in microfluidic flows. Phys Fluids 16(11):4028–4034.

Picioreanu C, van Loosdrecht MCM, Heijnen JJ. 2000a. Effect of diffusive and convective substrate transport on biofilm structure formation: A two-dimensional modeling study. Biotechnol Bioeng 69(5):504–515.

Picioreanu C, van Loosdrecht MCM, Heijnen JJ. 2000b. A theoretical study on the effect of surface roughness on mass transport and transformation in biofilms. Biotechnol Bioeng 68(4):355–369.

Qi Pa, Hou YJa. 2006. Mud mass transport due to waves based on an empirical rheology model featured by hysteresis loop. Ocean Eng 33(16):2195–2208.

Rani SA, Pitts B, Stewart PS. 2005. Rapid diffusion of fluorescent tracers into *Staphylococcus epidermidis* biofilms visualized by time lapse microscopy. Antimicrob Agents Chemother 49(2):728–732.

Rupp CJ, Fux CA, Stoodley P. 2005. Viscoelasticity of *Staphylococcus aureus* biofilms in response to fluid shear allows resistance to detachment and facilitates rolling migration. Appl Environ Microbiol 71(4):2175–2178.

Seymour JD, Codd SL, Gjersing EL, Stewart PS. 2004a. Magnetic resonance microscopy of biofilm structure and impact on transport in a capillary bioreactor. J Magn Reson 167(2):322–327.

Seymour JD, Gage JP, Codd SL, Gerlach R. 2004b. Anomolous fluid transport in porous media induced by biofilm growth. Phys Rev Lett 93(19):8103–8106.

Shaw T, Winston M, Rupp CJ, Klapper I, Stoodley P. 2004. Commonality of elastic relaxation times in biofilms. Phys Rev Lett 93(9):8102–8105.

Stewart PS, Rani SA, Gjersing EL, Codd SL, Zheng Z, Pitts B. 2007. Observations of cell cluster hollowing in *Staphylococcus epidermidis* biofilms. Lett Appl Microbiol 44(4):454–457.

Stoodley P, Debeer D, Lewandowski Z. 1994. Liquid flow in biofilm systems. Appl Environ Microbiol 60(8):2711–2716.

Sutherland IW. 2001. Biofilm exopolysaccharides: A strong and sticky framework. Microbiology 147:3–9.

Takenaka S, Trivedi HM, Corbin A, Pitts B, Stewart PS. 2008. Direct visualization of spatial and temporal patterns of antimicrobial action within model oral biofilms. Appl Environ Microbiol 74(6):1869–1875.

Towler BW, Cunningham A, Stoodley P, McKittrick L. 2007. A model of fluid-biofilm interaction using a Burger material law. Biotechnol Bioeng 96(2):259–271.

Vogt M, Flemming H-C, Veeman WS. 2000. Diffusion in *Pseudomonas aeruginosa* biofilms: A pulsed field gradient NMR study. J Biotechnol 77:137–146.

Xavier JB, Picioreanu C, Rani SA, van Loosdrecht MCM, Stewart PS. 2005. Biofilm-control strategies based on enzymic disruption of the extracellular polymeric substance matrix—A modeling study. Microbiol 151:3817–3832.

Ziebis W, Foster S, Huettel M, Jorgensen BB. 1996. Complex burrows of the mud shrimp *Callianassa truncata* and their geochemical impact in the sea bed. Nature 382(6592):619–622.